# Significant Response of Methane in the Upper Troposphere to Subseasonal Variability of the Asian Monsoon Anticyclone

Sihong Zhu[1], Mengchu Tao[1,2*], Zhaonan Cai[1,3], Yi Liu[1,3,4], Liang Feng[5,6], Pubu Sangmu[7], Zhongshui Yu[8], Junji Cao[9]

[1]Carbon Neutrality Research Center, Institute of Atmospheric Physics, Chinese Academy of Sciences, Beijing 100029, China
[2]Key Laboratory for Middle Atmosphere and Global Environment Observation, Institute of Atmospheric Physics, Chinese Academy of Sciences, Beijing 100029, China
[3]Key Laboratory of Atmospheric Environment and Extreme Meteorology, Beijing 100029, China
[4]University of Chinese Academy of Sciences, Beijing 100049, China
[5]National Centre for Earth Observation, University of Edinburgh, Edinburgh, EH9 3FF, UK
[6]School of GeoSciences, University of Edinburgh, Edinburgh EH9 3FF, UK
[7]Linzhi City Meteorological Bureau/CMA Mêdog Field Observatory for Atmospheric Water Cycle, Linzhi, 860000, China
[8]Xizang Institute of Plateau Atmospheric and Environmental Science Research/Xizagê National Climate Observatory, Lhasa, 850001, China
[9]Institute of Atmospheric Physics, Chinese Academy of Sciences, Beijing 100029, China

*Correspondence to*: Mengchu Tao (mengchutao@mail.iap.ac.cn)

**Abstract.** Substantial methane ($CH_4$) emissions in Asia are efficiently transported to the upper troposphere through the monsoon dynamical system, which forms a remarkable seasonal $CH_4$ enhancement in the upper troposphere. Using a chemical transport model GEOS-Chem driven by surface optimized $CH_4$ flux, the $CH_4$ enhancement over the Asian monsoon region is explored as a combined effect of the monsoon dynamical system and regionally increased emissions during late monsoon season. The spatial distributions of $CH_4$ at the upper troposphere show strong subseasonal variability, which is closely tied to the east-west oscillation of Asian monsoon anticyclone (AMA). Besides, the AMA patterns influence the efficiency ~~vertical structure~~ of methane-rich air transport to the upper troposphere and lower stratosphere~~methane~~. The AMA center around 80°E favors the upward transport from organized monsoon convective sources over the Indian subcontinent and Bay of Bengal ~~north India and Bangladesh~~ while the AMA center around 105°E favors the source from southwest China transported to the upper troposphere. When the AMA shifts over the Iranian Plateau, ~~The AMA center over the Iranian Plateau suppresses the~~ vertical transport from the convective outflow level further to the upper troposphere is weakened and ~~favors~~ the horizontal redistribution becomes dominant. According to our model sensitivity study, the differences in the upper tropospheric $CH_4$ anomalies caused by large-scale circulation is 1-2 times of that caused by regional surface emissions. Our research highlights the complex interaction between monsoon dynamics and surface emissions to determine the upper tropospheric methane.

# 1 Introduction

Methane (CH$_4$), the second most important greenhouse gas, emitted heavily from south Asia and China, accounts for ~25%
of the global anthropogenic emission budget in the recent decades (Stavert et al., 2022). The Asian summer monsoon (ASM) has been proven to be an efficient pathway connecting the rich methane boundary layer and the upper troposphere and lower stratosphere (UTLS) (Randel et al., 2010). The CH$_4$ enhancement in the UTLS ~~upper atmosphere~~ impacts the climate through radiative forcing (Riese et al., 2012) and influences the stratospheric chemistry, e.g., the methane oxidation (Rohs et al., 2006). More critically, limited understanding of non-local methane sources might mislead the flux inversion from total columns from satellite products (Zeng et al., 2021).

Observations (satellite retrievals and in-situ measurements) and models have evidenced remarkable enhancements of tropospheric tracers over the ASM region in the UTLS, including CO, water vapor, HCN and hydrocarbons, and aerosols (Bucci et al., 2020; Park et al., 2009; Pan et al., 2016; Pan et al., 2024; Randel et al., 2010; Rosenlof et al., 1997; Yu et al., 2017). Similar like other tropospheric tracers, substantial observational evidence showed distinct spatiotemporal distribution of high methane in the middle to upper troposphere over the Asian region during the late monsoon season (Baker et al., 2012; Schuck et al., 2010; Tao et al., 2024; Tomsche et al., 2019) as well as its lasting and traceable pathways into the southern hemisphere and the stratosphere after monsoon withdraw (Belikov et al., 2022; Yan et al., 2019).

The ASM transport structure connecting the surface source regions and the Asian monsoon anticyclone (AMA) in the UTLS has been characteristically described by various studies. The transport system is marked by deep convection, rapidly injecting surface air masses up to ~~into the UTLS, reaching~~ the convective outflow level, potential temperature heights ~~around~~ 360 K (~16 km) ~~within hours,~~ which commonly refers to "fast convective chimney" (Pan et al., 2016). Above 370 K, the continuous upward transport is mainly ~~Superimposed on the anticyclonic flow,~~ an anticyclonic ~~slow~~ "spiraling" movement ~~diabatic heating with a vertical velocity of about 1-1.5 K/day leads to an upward spiraling movement of air parcels~~ (Bergman et al., 2013; Lau et al., 2018~~; Pan et al., 2016~~; Ploeger et al., 2017; Vogel et al., 2019) along with a slow upwelling in a vertical velocity typically 0.3~0.8 K/day (Garny and Randel, 2016; von Hobe et al., 2020; Legras and Bucci, 2020; Vogel et al., 2024). Significant deep vertical transport is predominantly observed in the southeastern quadrant of the anticyclone, centered near the southern flank of the Tibetan Plateau. This ~~region acts as a~~ "chimney-like transport" actively uplifts~~', where~~ air from the highly-polluted regions, like northeast India, Nepal, and the northern Bay of Bengal, ~~boundary layer is rapidly lifted~~ to the upper troposphere~~tropopause level, facilitated by vigorous convection over areas like northeast India, Nepal, and the northern Bay of Bengal~~. Thi~~s~~e rapid convective uprising process was further characterized by a 'double-stem-chimney cloud' (Lau et al., 2018) or 'two-stem mushroom' (Pan et al., 2022) structure, which indicates two key areas prominently contributing to the "fast convective chimney"~~upward transport~~: the Himalayas-Gangetic Plain and the Sichuan Basin in southwestern China.

One key dynamical feature for the ASM is its subseasonal variability, which is characterized by the active–break cycle of precipitation and surface pressure patterns (Krishnamurti and Ardanuy, 1980; Krishnamurti and Bhalme, 1976), as well as

the east-west oscillation of AMA (Nützel et al., 2016; Zhang et al., 2002) with eddy shedding of low potential vorticity (PV) air in the UT (Garny and Randel, 2013). The variability in the monsoon convection pattern potentially modulates the intensity and position of the AMA (Garny and Randel, 2013; Nützel et al., 2016; Siu and Bowman, 2020). Moreover, the combined effects of convective uplift and anticyclonic confinement jointly shape the distribution and transport of tracers such as CO in the UTLS, as demonstrated and analysed in previous studies (Luo et al., 2018; Pan et al., 2016).

According to simulations with chemical transport models as well as the satellite observations, it is evident that the CH$_4$ the CH$_4$ enhancement in the upper troposphere (UT), similar as tracer like CO and water vapor, also has an isolated center over Asian monsoon region during the boreal summer (Park et al., 2004, Tao et al., 2024; Xiong et al., 2009). This increase of CH$_4$ is about 100 ppb higher than its regional annual mean volume mixing ratio (VMR) and is 3%~10% higher than the VMRs averaged over the same latitude varies from 3% to 10% (Park et al., 2004;(-Tao et al., 2024; Xiong et al., 2009). The relevant studies rarely use CH$_4$ as monsoon transport tracer due to its complicated emission sources. Different from tracer like CO, that has primarily industrial sources and hence displays little seasonal variation, CH$_4$ emissions in Asia, predominantly (over 60%) from rice cultivation (Stavert et al., 2022), exhibit significant seasonality. The debate persists over which factor plays the dominant role in whether the seasonal increase of UT methane overin the Asian monsoon region— is due to enhanced summer emissions from regional rice paddies (Zhang et al., 2020) or the strong upward transport by the monsoon convection and al circulation (Zeng et al., 2021) —as both are known to contribute. Hence, it is crucial to understand how the lower boundary methane conditions and monsoon circulation interact with each other.

The purpose of this study is (1) to explore the association of UT methane over ASM with subseasonal variability of AMA dynamics and (2) quantify the relative role of the AMA dynamics and regional emissions in shaping UT methane. The state-of-the-art approach for the goal is model simulations with a data assimilation system. The reasonable representation of UT CH$_4$ over ASM with this model has been proven through a comprehensive comparison with satellite and in-situ observations in a previous study (Tao et al., 2024). In this study, we first show the subseasonal behaviour of UT methane modulated by the AMA using the case of summer 2020. Then, we analyze the methane transport pathways under different AMA modes through mode composites. Lastly, we examine the UT methane change in association with AMA dynamics and surface emission respectively, through a model sensitivity study.

## 2 Data and Method

### 2.1 Global 3-D methane simulation

We use v12.5.0 of GEOS-Chem (http://www.geos-chem.org, The International GEOS-Chem User Community, 2019) to generate of global 3-D methane concentrations for the study period 2015–2020, with a temporal resolution of 1 day and a spatial resolution of $2° × 2.5°$ (longitude × latitude). The model is driven by the Modern-Era Retrospective Analysis for Research and Applications version 2 (MERRA-2) re-analysis from the Global Modelling and Assimilation Office of NASA

(Gelaro et al., 2017), which also provides the convective mass fluxes used to represent convection. For consistency, we also use MERRA-2 reanalysis data to analyze dynamical fields.

The surface CH$_4$ fluxes used in the transport model are optimized with atmospheric observations via an ensemble Kalman Filter (EnKF) framework (Feng et al., 2009, 2017). In the framework, the *a priori* emission estimates include natural sources (e.g., wetlands, fires, termites), and anthropogenic sources (e.g., fossil fuels, livestock, rice, and waste) as detailed in Zhu et al., (2022). The atmospheric CH$_4$ observations include the proxy GOSAT v9.0 column methane data (XCH$_4$) from the University of Leicester (https://catalogue.ceda.ac.uk/uuid/18ef8247f52a4cb6a14013f8235cc1eb/, Parker et al., 2020) and near-surface methane mole fraction samples from the CH$_4$ GLOBALVIEWplus v5.0 ObsPack (https://gml.noaa.gov/ccgg/obspack/release_notes.html#obspack_ch4_1_GLOBALVIEWplus_v5.0_2022-10-17, Schuldt et al., 2022).

The inverted flux-driven global 3-D methane concentrations were evaluated using observations from several platforms, including ground-based XCH$_4$ measurements from the Total Carbon Column Observing Network (TCCON) (https://tccondata.org/, TCCON Team, 2022), CH$_4$ flask samples collected by aircraft in the Comprehensive Observation Network for TRace gases by AIrLiner (CONTRAIL) project (https://www.cger.nies.go.jp/contrail/index.html, Machida et al., 2023) and CH$_4$ profiles from ground to 25 km measured over the Tibetan Plateau by an AirCore air sampling and data processing system (Tao et al., 2024). In our simulation experiments, only surface CH$_4$ flux is varied, with no alterations to meteorological fields or initial conditions.

## 2.2 Classification of Asia monsoon anticyclone modes

In a series of previous studies, the subseasonal variability of AMA has been mainly characterized as 'bimodality', referring to two major modes: Tibetan mode and Iranian mode (Nützel et al., 2016; Zhang et al., 2002). It is important to note that However, the existence and nature of this bimodality remain a topic of ongoing debate. For instance, Nützel et al. (2016) demonstrated that the bimodal distribution of the AMA center is sensitive to the choice of reanalysis datasets. Manney et al. (2021) also proposed, with some study arguing that the bimodality is not a prominent feature for the AMA climatological state (Manney et al., 2021). OIt is important to note that our study does not aim to confirm the existence of AMA bimodality or to explore its underlying dynamics. We aim to investigate the relationship between AMA subseasonal variability and the three-dimensional distribution and transport of methane.

To identify the AMA major center, we use wind and geopotential height (GPH) data from MERRA-2 reanalysis and basically follow the methodology outlined in Zhang et al. (2002) as shown in Figure 1. The AMA centers are identified as the positions of GPH peaks (magenta crosses in Fig.1) along the ridgeline of anticyclone (zero u-wind within the ASM region, i.e. 30°W-180°E, 10°N-40°N, shown as blue dotted line in Fig. 1) on daily basis. We exclude centers with GPH values in the lowest 70% of the GPH range measured along the ridgeline. Different from previous studies that commonly use 100 hPa as a reference, we use the 150 hPa pressure level because both convection-driven vertical uplift and horizontal

confinement are active at this layer, providing significant variability in AMA and its impact on transport of tracer gases.
Meanwhile, the anticyclonic circulation basically remains closed at 150 hPa.

As shown in Fig. 1(d), our statistics on the probability distribution of AMA center positions is based on days with a single center during 6 boreal summers (July, August and September, JAS) from 2015 to 2020. The distribution exhibits a pattern resembling bimodality, though it is less distinct than that reported in Zhang et al. (2002). The frequency of the Tibetan mode (the eastern phase of the distribution) is nearly twice that of the Iranian mode. Furthermore, within the Tibetan Plateau (TP) cases, we find a weaker bimodal structure with one peak located to the west of 90°E and another to the east.
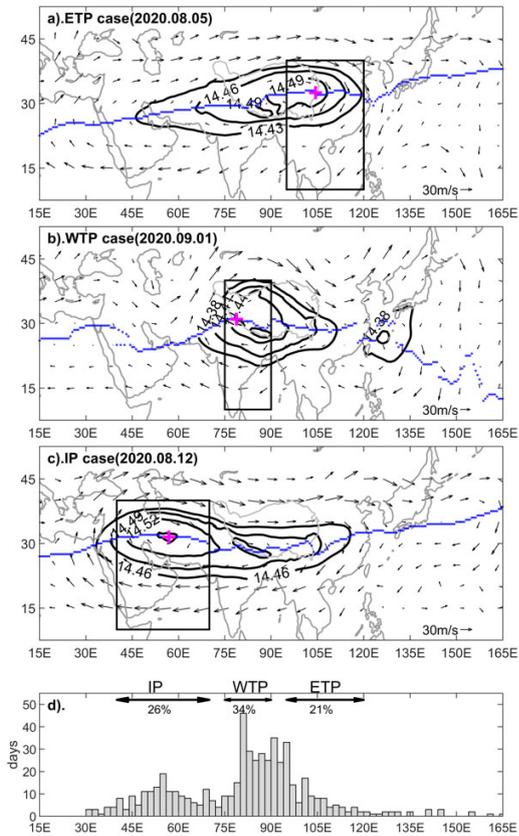
**Figure 1: The daily meteorological maps are shown as three mode cases in panels (a-c), including horizonal wind field (arrows) and geopotential height (GPH, black contours) on 150 hPa. The blue dotted line denotes the zero u-wind, indicating the ridgeline of anticyclone. The magenta cross marks the local GPH peaks along the ridgeline, which is identified as AMA center. The distribution of the AMA major center along the longitudes is shown in panel (d). This statistic includes the daily meteorological data covering 6 boreal summers (July, August and September) from 2015 to 2020. The frequencies of occurrence (%) for the three AMA modes are also labeled. The rectangle in (a-c) outlines the geographic domain corresponding to each mode.**

~~To identify the AMA major center, we use wind and GPH data from MERRA-2 reanalysis and basically fFollowing the methodology outlined in Zhang et al. (2002) as shown in Figure 1., Tthe AMA centers are identified as the positions of geopotential height (GPH) peaks (magenta crosses in Fig.1) along the ridgeline of anticyclone (zero u-wind within the ASM~~

region, i.e. 30°W-180°E, 10°N-40°N, shown as blue dotted line in Fig. 1zero u-wind within the ASM region (30°W-180°E, 10°N-40°N)) on daily basis using wind and GPH from MERRA-2 reanalysis. We exclude centers with GPH values in the lowest 70% of the GPH range measured along the ridgeline. Different from previous studies that commonly use 100 hPa as a reference, we use the 150 hPa pressure level because both convection-driven vertical uplift and horizontal confinement are active at this layer, providing significant variability in AMA and its impact on tracer transport of tracer gases. Meanwhile, the anticyclonic circulation basically remains closed at 150 hPa.

As shown in Fig. 1(d), oOur statistics on the probability distribution of AMA center positions is based on days with a single center during 6 boreal summers (July, August and September, JAS) from 2015 to 2020. The probability distribution of AMA center positions in our study exhibits a pattern resembling bimodality, though it is less distinct than that reported in Zhang et al. (2002). Tshow that the frequency of the Tibetan mode (the eastern phase of the distribution) is is nearly twice that of the Iranian mode. Furthermore, within the Tibetan Plateau (TP) cases, we find a weaker bimodal structure with one peak located to the west of 90°E and another to the east.Anomalies of GPH and CH4 concentrations in this study are defined as deviations from the daily mean values averaged over the main Asian Summer Monsoon (ASM) region (15°N-40°N, 15°E-135°E). The enhancement of XCH4 or CH4 within each pressure layer is expressed as a percentage relative to the corresponding zonal mean at each latitude: enhancement (%) = [(XCH4 – zonal mean XCH4) / zonal mean XCH4] × 100, where the zonal mean is computed at each pressure level across the longitudinal band.Additionally, we observe a less pronounced bimodal feature within Tibetan Plateau (TP) cases, prompting us to further subdivide the Tibetan mode into the East Tibetan Plateau mode and the West Tibetan Plateau mode, based on the AMA's position relative to the longitudinal meridian of ~90°E (the center of heating in the TP). Nützel et al. (2016) proposed that due to the continuous spatial variability of the AMA center and its connection to convective activity, a more flexible classification approach should be adopted rather than relying on a fixed bimodal structure. Variations in regions of enhanced convection and associated changes in AMA morphology potentially influence the distribution of upper tropospheric tracers through vertical transport and anticyclonic confinement (e.g. Pan et al., 2016; Tomsche et al. 2019; Vogel et al., 2019). Based on this perspective, our study further subdivides the Tibetan Plateau (TP) mode into the East Tibetan Plateau (ETP) and West Tibetan Plateau (WTP) modes. Consequently, we define three AMA modes in total: the Iranian Plateau (IP) mode (40–70°E), WTP mode (75–90°E), and ETP mode (95–120°E). Previous study has also noted the different effects of the AMA being centered on the east or west side of the Tibetan mode on upper tropospheric tracers and thus introduced more classification (Tomsche et al., 2019). This classification also aligns with our subsequent analysis of the corresponding source regions.

The AMA modes are therefore classified according to the number and position of AMA center(s) on a daily basis for six boreal summers (July, August and September, JAS) from 2015 to 2020. Dates with a single center are categorized by the longitudinal position of the center: 40-70°E defining as the Iranian Plateau (IP) mode, 75-90°E as West Tibetan Plateau (WTP) mode, and 95-120°E as East Tibetan Plateau (ETP) mode.

**3 Results**

180 **3.1 Subseasonal variability in upper tropospheric CH$_4$ during 2020 Asian summer monsoon**

We firstly examine the covariability ~~influence~~ of the large-scale circulation of ASM and~~on~~ the horizontal distribution of ~~GPH and~~ CH$_4$ at 150 hPa ~~during~~using the case in the summer of 2020.~~the vertical distribution of CH$_4$ in 2020 summer.~~ Figure 2 (a-b) presents Hovmöller diagrams of ~~GPH and CH$_4$ anomalies on 150 hPa ~~, calculated relative~~referring ~~to their respective daily means averaged over the core ASM region (15°N–40°N, 15°E–135°E). ~~Hovemoller diagram shows the~~

185 ~~anomalies of GPH as well as methane on 150 hPa refer to their daily means over the main ASM region (15°N 40°N, 15°E 135°E; Figure 1).~~ The AMA experienced four~~4~~ east-west oscillations from July to mid-August and ~~(Figure 1a), commencing with a positive GPH anomaly around 85°E 90°E – attributable to thermal heating in the TP – followed by a westward migration due to instability. From mid August, the AMA center over predominantly hovered east of 75°E. These subseasonal variability of AMA has a pronounced influence on the distribution of CH$_4$ in the middle to upper troposphere~~

190 ~~(see Figure 1b). Simulated CH$_4$ is highly correlated (r = 0.78) with the geopotential height field. These oscillations initiated with a positive GPH anomaly centered around 85°E 90°E, likely driven by thermal forcing over the Tibetan Plateau, and subsequently migrated westward due to dynamical instabilities (Citation). From mid August onwards,~~ the AMA center remained predominantly east of 75°E from mid-August onwards (Figure 1a). ~~This subseasonal variability of the AMA exerts a substantial impact on the distribution of CH$_4$ in the middle to upper troposphere, as illustrated in Figure 1b.~~ The simulated

195 CH$_4$ anomalies display a strong spatial correlation with the GPH field, with a Pearson correlation coefficient of 0.78. This subseasonal variability of AMA significantly modulated the CH$_4$ variations in the middle to upper troposphere (see Figure 1b), similar to the behavior of tracers such as CO (Pan et al., 2016), primarily due to anticyclonic confinement (Ploeger et al., 2015).
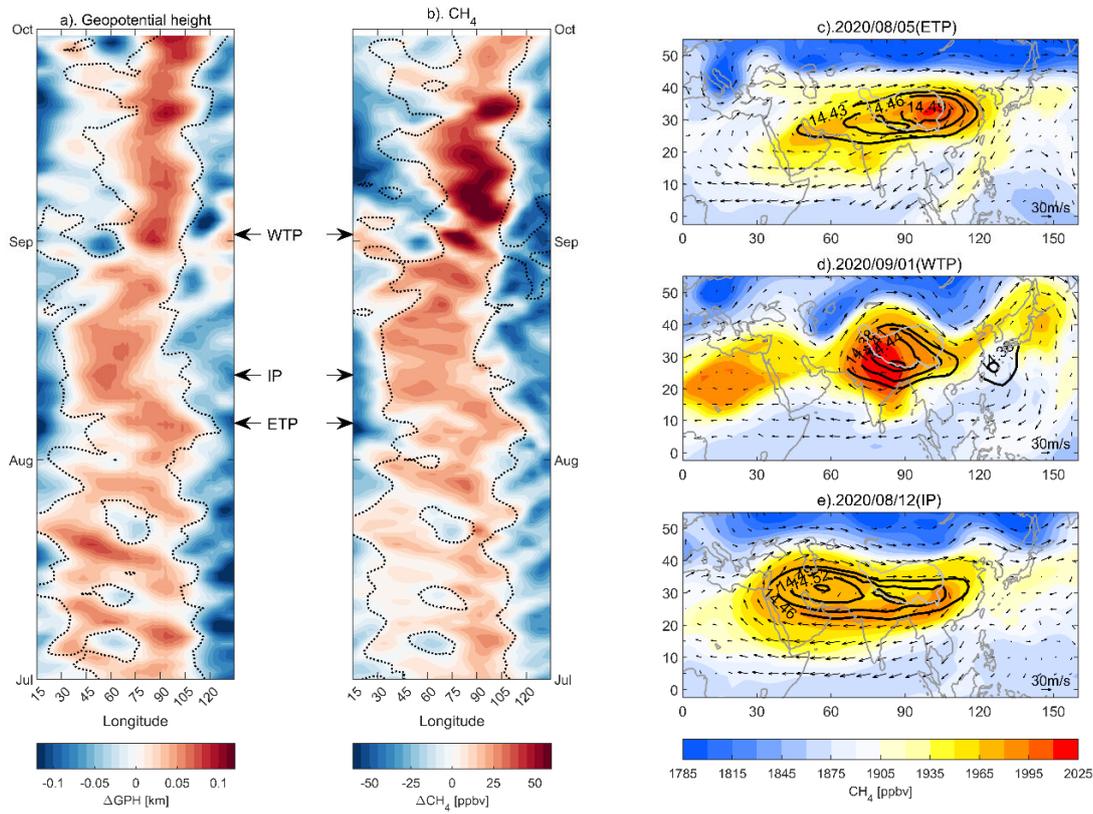
**Figure 2: Hov~~e~~möller diagrams of anomalies in (a) geopotential height and (b) CH₄ concentrations at 150hPa for JAS 2020. Anomalies are calculated with respect to ~~as deviations from~~ the daily mean values averaged over the main ASM region (15°N–40°N, 15°E–135°E). The zero-contour (dotted line) of each panel is plotted on opposite filed for reference. The Pearson correlation coefficient between the two anomaly fields is 0.78. Panels (c-e) show maps of daily mean CH₄ concentration at 150hPa (color shades) for three selected days (indicated by arrows in the Hovmöller diagrams), representing characteristic states for~~of~~ the WTP, IP and ETP mode of AMA subseasonal oscillation. Black contours denote selected geopotential height levels highlighting the AMA ~~-~~center, and vectors represent the horizontal wind field at 150 hPa.**

The east-west migration of $CH_4$ anomalies mirrors the subseasonal oscillations of the AMA on daily basis, revealing the dynamic nature of methane distribution over monsoon region. Hereby we select 3~~4~~ days to illustrate the spatial distribution of methane and dynamical fields under the three~~typical~~ AMA modes in Fig.~~ure~~ 1(c-e)~~2~~: East Tibetan Plateau (ETP) mode centering 90°E-110°E (Aug. 5th), ~~Iranian Plateau (IP) mode centering 50°E-60°E (Aug. 12th), double center mode (Aug. 30th) and~~ West Tibetan Plateau (WTP) mode centering 80°E-90°E (Sep. 1st~~8th~~) and Iranian Plateau (IP) mode centering 50°E-60°E (Aug. 12th). The daily maps show that although the high $CH_4$ ~~anomaly enhancement~~ was largely confined within AMA, $CH_4$ peak does not invariably align with the AMA center. For example, at IP mode on Aug. 12st ~~(see Figure 2b)~~, the high methane center locates southern edge of AMA. This pattern results from the "stirring" interaction between convection-uplifted boundary layer air from the Indian subcontinent (as shown by the overlap between the main monsoon convection source and high methane regions near the lower boundary in Fig. S1) and the surrounding air, which is similar like "stirring" interaction proposed by Pan et al. (2016).~~, which results from "stirring" interaction between uplifted boundary layer air and surrounding air.~~
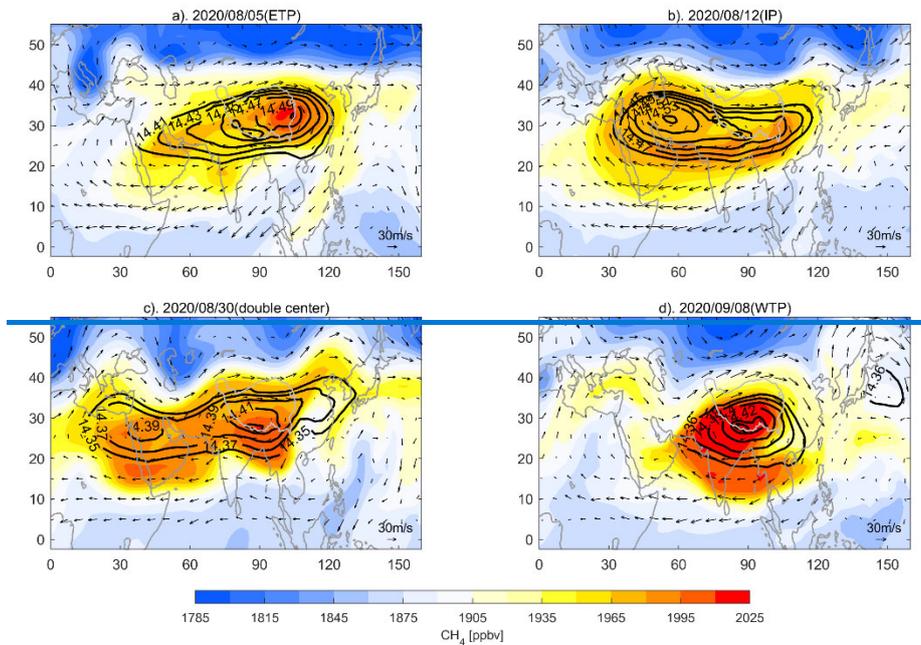
The subseasonal dynamical control of AMA on $CH_4$ in the middle to upper troposphere is similar as other tracer like CO (Luo et al., 2018; Pan et al., 2016). Contrasting with CO—which typically shows a significant increase in UT around mid-June, correlating with the onset of the South Asian monsoon and its associated convective transport—we observe a pronounced increase in $CH_4$ concentrations at UT starting from~~in~~ mid-August, e.g. notably $CH_4$ increase within the 75°E-110°E longitudinal range in Fig.~~ure.~~1(b). The timing of this ~~CH₄~~ $CH_4$ surge aligns closely with the seasonal emission ~~emissions~~ peak~~–~~ mainly from the rice paddy cultivation as suggested by Zhang et al. (2020)~~in emissionsfrom rice paddy cultivation, as indicated by the blue line in Figure 5a~~.

Observed the methane behavior throughout this summer, the monsoon large-scale circulation dynamics with a strong subseasonal variability clearly manipulate the spatial distribution of upper tropospheric $CH_4$, which is similar as tracers like CO and water vapor. Meanwhile, the temporal subseasonal variation of the mean $CH_4$ concentrations over AMA (a remarkable integral rise during mid-August and September) potentially relates to increased emissions in late monsoon season.

### 3.2 Composites of AMA modes

To extend the 2020 summer case to a general picture of $CH_4$ distribution under different AMA status, we composite the methane daily fields for 6 summers (JAS during 2015-2020) according to the corresponding AMA modes (see the Method section for the classification). According to the limited statistical samples, we found that IP mode predominantly manifests

during Julys, while the ETP mode is more frequently observed in Septembers. This phenomenon is also observed in the 2020 case as shown in Figure 1. Figure 3 presents the vertical structure of methane (longitude-pressure cross section) associated with three single-center modes (WTP, ETP and IP mode). It reveals that high concentrations of methane in the boundary layer are localized between 60°E to 105°E and undergo a redistribution to a broader area in the upper troposphere (300-100hPa).

This distribution emerged with the "double-stem-chimney cloud" or "two-stem-mushroom" structure, as characterized by (Lau et al., 2018; Pan et al., 2022), i.e., the two narrow "stems" (centered on 80°E and 105°E, respectively) indicating vertical pumping by deep convections as well as the "cap" resulting from the expanding the uplifted near-surface air masses through quasi-isentropically transport. The composites add details to the "two-stem-mushroom" structure. The WTP mode favors the vertical uplifting over 80°-90°E (western "stem") while the ETP mode favors the vertical transport over 100°-110°E (eastern "stem"). Under IP mode, the horizontal horizonal redistribution is remarkable with a weak vertical pathway. Previous study has identified two key regions in connection with these two transport "stems": one is the Himalayas-Gangetic Plain mainly including the northern Indian region and Bangladesh, i.e. Indian subcontinent, and another one is southwest China (Lau et al., 2018, see also the surface flux map for monsoon season in Figure S1). As shown in Fig. 3(c), $CH_4$ enhancement in the upper troposphere under the IP mode is weaker than in the WTP and ETP modes. The underlying reason is not straightforward; it may result from weaker vertical uplift due to weaker convection in IP mode, a shift of the main convection to regions with lower emissions, and/or the position of the AMA center favoring horizontal redistribution over further vertical upwelling.

To further explore this, Figure 4 presents horizontal views at multiple layers to illustrate the relationship between convective sources and $CH_4$ enhancement in the upper troposphere for each AMA mode. Note that the $CH_4$ enhancement in Fig. 4 is expressed as a percentage (%) relative to the global zonal mean at each latitude band within each pressure layer. The corresponding $CH_4$ VMR absolute values can be found in Fig. S2.
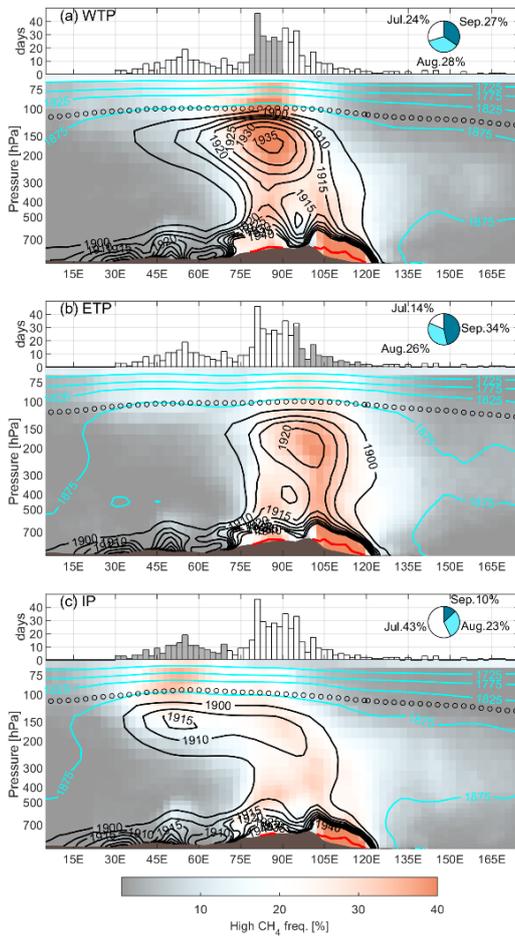
265

**Figure 3: Composites of the longitude-pressure cross section of methane (averaged over 15°N-40°N) for the three modes (2015-2020 JAS). The contours show the averaged methane volume mixing ratios (VMRs) for each mode (VMRs less than 1900ppbv shown as cyan contours and VMRs equal or greater than 1900ppbv shown as black contours). The color shades indicate the occurrence frequency (unit: %) of high CH$_4$ VMR (criteria: higher than 90% of grids within the Asian monsoon region on the**
270 **same model level). The longitude distribution of GPH maximum along the anticyclone ridge is plotted on the top of each panel, where the grey bars cover the longitude range for corresponding mode. The pie charts show the proportions of months for each mode.**

~~Figure 4 further shows horizontal view for the conjunction of source regions with CH₄ enhancement in the UT.~~ As being ~~The current findings suggest~~suggested by Fig. 3, ~~that~~ the horizontal maps confirm that the WTP mode facilitates the vertical
275 transport ~~first~~ from southern side of TP ~~pathway~~ to the UT (see Fig.~~ure~~ 4 left column, a1-a3), whereas the ETP mode is more conducive to promoting the vertical transport over eastern side of TP ~~second pathway~~ (Fig.~~ure~~ 4 middle column, b1-b3). The IP mode composite ~~(Figure 4 right column, c1-c3)~~ demonstrates that while UT methane enhancement is observed between 45°E to 60°E (Fig. 4 right column, c3), the corresponding enhancement at the middle troposphere ~~boundary layer~~ is located similarly to the TP modes, i.e., ~~specifically,~~ at the southern flank~~edge~~ of the Tibetan Plateau (Fig. 4 c3).

280 ~~This suggests that the UT enhancement during the IP mode is not primarily a result of direct vertical pumping but rather a complex redistribution involving the boundary layer air within the ambit of the AMA.~~Comparing the three bottom panels, we find that differences in $CH_4$ distribution within the lower troposphere among the three modes are minor. The occurrence of deep convection (shown as magenta contours, outgoing longwave radiation less than 210K) together with high methane emissions (bottom row in Fig. 4) jointly determine the methane distribution in the mid-troposphere (third row in Fig. 4). For

285 example, in both the WTP and IP modes, deep convection is enhanced over the southern flank of the TP, where methane emissions are intense, resulting in a mid-tropospheric methane enhancement in this region (Fig. 4 a3 & c3). In contrast, during the ETP mode, convection is suppressed over the Indian subcontinent but get active over southwestern China, causing the high methane center to shift to southwestern China (Fig. 4b3). It is also notable that these convective sources with elevated methane are subject to redistribution and confinement by the anticyclonic circulation in the upper troposphere (100–

290 300 hPa).
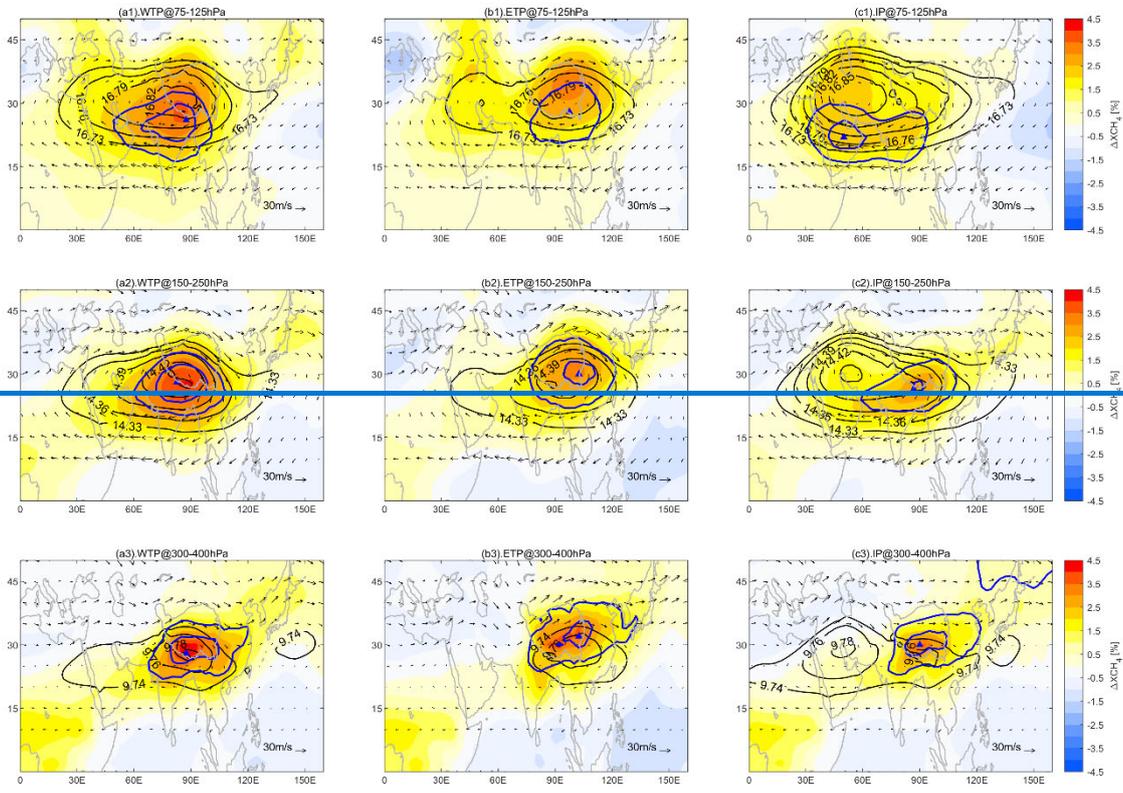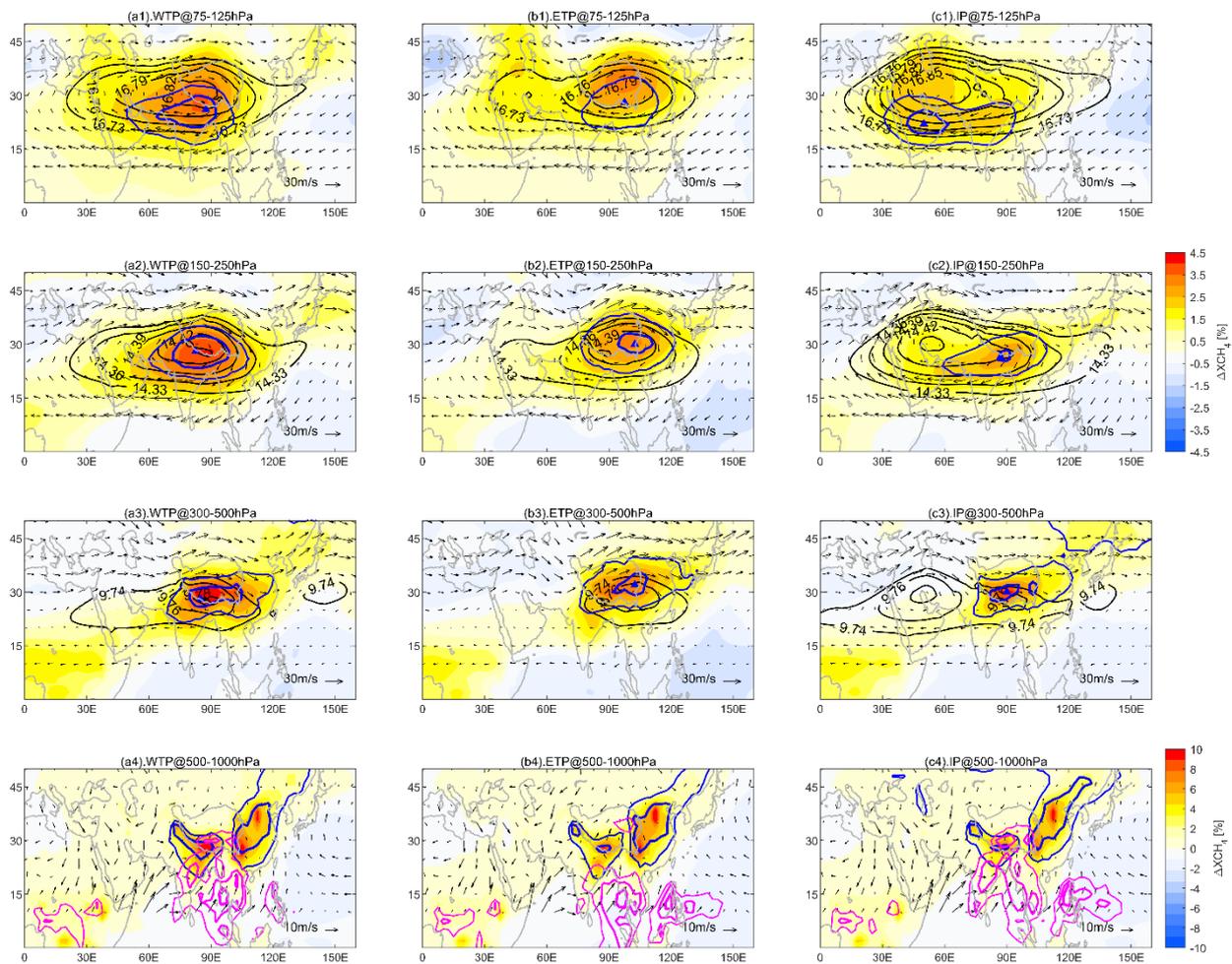
Figure 4: Horizonal distribution of XCH$_4$ anomaly composites corresponding to the three dominant AMA modes, shown across 4 vertical layers: the lowermost stratosphere (75–125 hPa; top panels a1–c1), the upper troposphere (150–250 hPa; panels a2–c2), the middle troposphere (300–400 hPa; panels a3–c3), and the lower troposphere (500–1000 hPa; bottom panels a4–c4). Color shading indicates the XCH$_4$ anomalies, expressed as a percentage (%) relative to the global zonal mean at each latitude within each pressure layer. Black contours depict the GPH field outlining the AMA structure. Blue lines enclose regions with high occurrence frequencies (50% and 70%) of elevated methane—defined as in Figure 3—and triangles mark the locations with highest occurrence frequency. Magenta contours indicate outgoing longwave radiation (OLR) composites lower than 210 K for each mode, with an interval of 10 K, which represents the deep convective cloud.

Figure 4: Horizonal distribution of the 3 three mode composites at the low troposphere (500-1000 hPa, bottom panels a4-c4) the middle troposphere (300-400hPa, third bottom panels a3-c3), the upper troposphere (150-250hPa, middle second panels a2-c2) and the lowermost stratosphere (75-125hPa, top panels a1-c1). The color shades show the XCH$_4$ anomalies enhancement (unit: %, referring to zonal mean) within the concern pressure range. The black contours indicate the AMA (GPH contours). The blue lines mark the region with high occurrence frequency (50% and 70% are plotted) of elevated methane (definition same as Figure 3) and the triangles mark the location with highest occurrence frequency.

It is suggested that the spatial relationship among surface emissions, convective uplift, and the extent of the AMA collectively shapes the upper tropospheric methane enhancement. Meanwhile, the configuration of ASM subseasonal dynamical variability, including both the monsoon convection and AMA locations, influences the efficiency of tracer transport from the lower boundary to the upper troposphere. The ~~Among the three composites, it is evident that the~~ WTP mode offers the most effective transport ~~pathway~~ for methane-rich ~~methane~~ air from Himalayas-Gangetic Plain to the UT because the main convective sources are injected near the center location of the AMA. The methane enhancement observed in the UT ~~during the WTP mode is nearly twice (4~5%) that observed in the IP mode~~ is only (about ~2% during the IP mode ) ~~and also stronger than ETP mode (~3%)~~ due to a ~~.~~ horizontal displacement between its main convective source region (Himalayas-Gangetic Plain) and the AMA. ~~According to the limited statistical samples, we also found that IP mode predominantly manifests during Julys, while the ETP mode is more frequently observed in Septembers. This phenomenon is also observed in the 2020 case as shown in Figure 1.~~

**3.3 Contribution from the emissions and dynamics of ASM system**

In Sections 3.1 and 3.2, we demonstrate that variability in UTLS methane over the Asian region is influenced by two main factors: firstly, the dynamical east-west oscillation of the ASM, which substantially modulates methane 3D-distribution and influence the efficiency of upward transport ~~pathways~~; secondly, the increase in methane emissions mainly from rice paddy cultivation in late August and early September, which potentially intensify the upper-level methane structure during the late monsoon season. In this section, we further quantify the contributions of these two factors—specifically, surface emissions and ASM dynamics—to regional methane enhancement, allowing us to assess their relative impact on methane variability in the UTLS.

Figure 5(a) presents the time series of total methane emissions (blue line) and methane concentrations in the UTLS (orange line), averaged over the ~~Asian summer monsoon (~~ASM~~)~~ region (15–40°N, 15–135°E). The results indicate that the annual maxima of UTLS methane concentrations generally coincide with the peaks in annual emissions. Furthermore, years exhibiting higher emissions during the JAS compared to other years ~~with higher late summer emissions~~ tend to correspond to elevated methane concentrations in the UTLS. For instance, during JAS ~~(July–September)~~ 2020, when seasonal emissions reached a relatively high value (~19.3 Tg for the entire ASM region), the UTLS methane concentration also peaked (~1928 ppbv), marking the maximum throughout the simulation period.

Meanwhile, we notice that the interannual variability of methane in the UTLS (orange line) during the monsoon season is 40% larger than other seasons, while the emissions during monsoon did not show remarkably larger interannual variability than other seasons. This suggests that upper level methane during monsoon season are not solely determined by emission magnitude but to some extend influenced by the ASM dynamical conditions or other factors. For example, while the seasonal total emissions during JAS 2016 and 2018 are comparable (18.3 Tg versus 18.4 Tg), the seasonal and regional mean methane concentration in the UTLS during JAS 2018 is ~30 ppbv (~1.5%) higher than in 2016, which is a remarkable

340 interannual difference. This difference can be attributed to variations in the distribution of anticyclone modes (Figure 5b &
Figure S2). Specifically, during JAS 2018, the ASM anticyclone exhibited a higher frequency of WTP (western Tibetan
Plateau) and ETP (eastern Tibetan Plateau) modes, particularly in August and September, creating a more favorable
configuration for upward transport compared to 2016. A detailed comparison of subseasonal oscillations of the AMA
between 2016 and 2018 is provided in the supplementary material (Figure S32). Note that the CH$_4$ interannual variability in
345 the UTLS can be related to other large-scale climate modes. For example, the relative low CH$_4$ in the UTLS in 2015 is
potentially attributed to suppressed updrafts influenced by ENSO-related dynamics (Alladi et al., 2024).
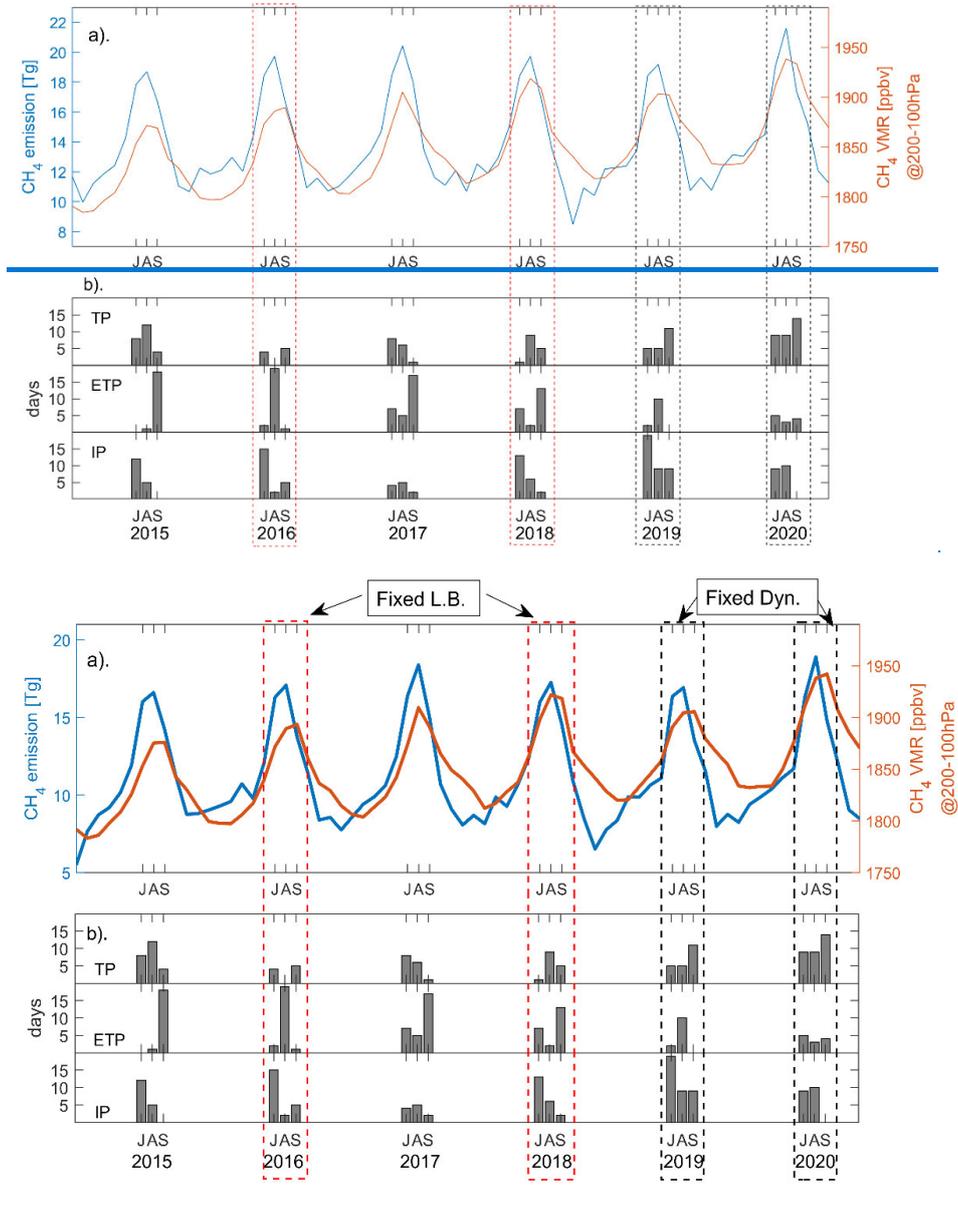
**Figure 5: a) Time series of monthly total methana ~~total~~ emission (unit: Tg) and VMRs (unit: ppbv) averaged over the ASM region (15-40°N~~N~~, 15-135°E~~E~~). (b) Number ~~The number~~ of days identified for three AMA modes during JJS ~~July, August and September~~ for each year. The dashed red and black boxes indicate the Fixed L.B. and Fixed Dyn experiments, respectively, as described in Table 1.**

Based on the analysis above, we assess the relative contribution of emissions in the lower boundary and AMA dynamics to the upper level methane through a sensitivity test. We use the AMA dynamics of 2016 and 2018 as representative cases to examine configurations that suppress or enhance UTLS transport, respectively. To isolate the impact of AMA configuration, we conducted a test simulation using the lower boundary emissions of 2016 combined with the meteorological data of 2018 to drive the model (16LB/18Dyn). The resulting change in methane concentrations, compared to the control run for 2016 (16Ctl), represents the effect of AMA dynamics. To confirm that these results are independent of the boundary conditions, we conducted a parallel test using the lower boundary emissions of 2018 combined with the meteorological data of 2016 (18LB/16Dyn). The methane changes were then compared to the control run for 2018 (18Ctl). We found that the results of 16LB/18Dyn-16Ctl and 18Ctl-18LB/16Dyn were nearly identical (see Table 1 and Figure ~~S3~~S4). Consequently, we use the 16LB/18Dyn - 16Ctl simulation to illustrate the influence of AMA dynamics in the following analysis.

Additionally, we use the lower boundary conditions of 2019 and 2020 as representative cases for low and high emissions over the ASM region, respectively. The total emissions over the ASM region during JAS 2020 are remarkably higher (1.3 Tg, ~7%) than those in 2019. To isolate the effect of emissions, we conducted a test simulation using the lower boundary emissions of 2020 with the meteorological data of 2019 (20LB/19Dyn) and compared the results to the control run for 2019. Similarly, we ran a test replacing the 2020 lower boundary with the 2019 emissions (19LB/20Dyn). We found that the differences due to variations in the lower boundary emissions remained relatively consistent when using different dynamical fields (see details in Figure ~~S4~~S5). Therefore, in the following analysis, we use the results from 20LB/19Dyn-19Ctl to illustrate the effect of surface emissions.

**Table 1. Seasonal (JAS) and ASM regional (15-40N, 15-135E) mean CH₄ VMR (unit: ppbv) in the UTLS (200-100hPa) for the control and test runs.**

| | Control run | | Test run~~s~~ | | Diff. (test-control) |
|---|---|---|---|---|---|
| | Configuration | $CH_4$ (ppb) | Configuration | $CH_4$ (ppb) | $\Delta CH_4$ (ppb/%) |
| Fixed L.B. | 16Ctl | 1883 | 16LB/18Dyn | 1903 | 20 ( 1.06%) |
| | 18Ctl | 1909 | 18LB/16Dyn | 1888 | -21 (-1.11%) |
| Fixed Dyn. | 19Ctl | 1899 | 20LB/19Dyn | 1912 | 13 ( 0.68%) |
| | 20Ctl | 1928 | 19LB/20Dyn | 1912 | -16 (-0.83%) |

~~Figures 6 and 7 illustrate the spatial distribution of the effects from monsoon dynamics and emission conditions, respectively. Quantitatively, monsoon dynamics introduce stronger variations in methane concentrations (1-2%) in the UTLS region compared to the changes driven by emissions, which are less than 1%. This difference arises because the impact of dynamics~~

380

**Figure 6: The seasonal (JAS) mean differences of CH$_4$ VMR due to anticyclone dynamics (represented by 2016LB/2018DYN minus 2016CTL). (a) Longitude-pressure cross section of CH$_4$ differences (averaged over 15N-40N). The horizonal distribution of CH$_4$ differences are shown for 70hPa (b1), 100hPa (b2), 250hPa (b3), 500hPa (b4). Contours show the methane VMR for two runs: black for 2016LB/2018DYN and blue for 2016CTL. The circles mark the tropopause for 2016 (blue) and 2018 (black).**

385 Figures 6 and 7 illustrate the spatial distribution of the effects from monsoon dynamics and emission conditions, respectively. Quantitatively, monsoon dynamics introduce stronger variations in methane concentrations (1–2%) in the UTLS region compared to the changes driven by emissions, which are less than 1%. This difference arises because the impact of dynamics is amplified in the UTLS region (Figure 6a), while the influence of emissions diminishes progressively from the surface to higher altitudes (Figure 7a).

390 As shown in Figure 6, changes in CH$_4$ concentrations driven by dynamical fields are significant in the mid-troposphere to lower stratosphere, with variations ranging from 10 to 40 ppbv. Notably, these dynamical-induced changes propagate toward the northern edge of the AMA in the UTLS. The dynamical-related methane anomalies extend northward into the lowermost stratosphere and eastward across the Pacific Ocean along the prevailing westerlies (see Figure S5S6).

In contrast, differences driven by emission conditions are more localized, concentrating in northern India and the Sichuan

395 Basin within the lower troposphere (Figure 7b4), regions identified as critical for upward transport in Sec. 3.2. As the

methane is transported upward into the upper troposphere, emission-related anomalies are redistributed and confined within the AMA region, as outlined by the GPH isolines (black contours) and do not significantly extend into the stratosphere.
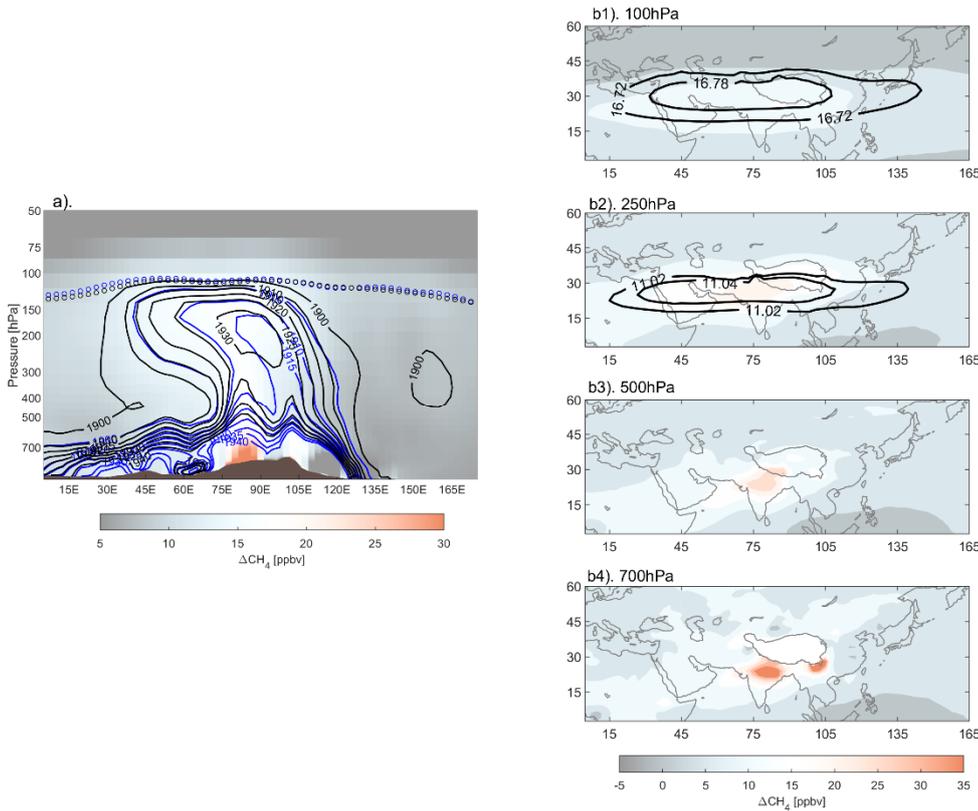
**Figure 7: Similar as Figure 6 but for differences of CH4 VMR due to emissions (represented by 2020LB/2019DYN minus 2019CTL). Contours show the methane VMR for two runs: black for 2020LB/2019DYN and blue for 2019CTL. And the black contours on (b1) &(b2) indicate the AMA (GPH contours).**

## 4 Discussions

The model results have a reasonable representation on the CH4 vertical and horizontal structure in comparison to the in-situ measurements and satellite datasets, which has been discussed in a previous study (Tao et al., 2024). The uncertainty in our simulation includes CH4 emission inversion uncertainty and modelling uncertainties such as representative error (Stanevich et al., 2020, 2021), transport scheme uncertainties (Bisht et al., 2021; Saito et al., 2013) and chemistry scheme uncertainties (Murray et al., 2021; Zhao et al., 2019). Here, the *a posteriori* CH4 fluxes used in our study show much larger interannual flux variations than the corresponding *a priori* estimates, with their uncertainties (<3%) typically 40% smaller than the *a priori* uncertainties.

Our study demonstrates two key findings: (1) the subseasonal oscillations of the AMA significantly influence the methane distribution ~~transport pathway~~ and its transport efficiency from the lower boundary to the UTLS ~~(upper troposphere and~~

~~lower stratosphere)~~; and (2) the interannual variations in methane enhancement in the UTLS are more strongly controlled by the conditions of AMA subseasonal oscillations than by emissions alone.

Notably, regional emissions, the organized monsoon convection as well as the ~~and~~ AMA modes ~~conditions~~ are not entirely
415 independent. On one hand, monsoon-driven heavy rainfall and resulting floods can increase methane emissions. ~~, Oand o~~n the other hand, the pattern of organized monsoon convection is coupled with AMA variations. One potential relationship is that upper level divergence caused by deep convection potentially shapes the AMA pattern. Therefore, further investigation is needed to understand the complex interactions among monsoon convection, regional emissions, and large-scale anticyclonic circulation, as well as how these interactions evolve under climate change.

420 **5 Conclusions**

Similar as tropospheric tracer like CO, spatial distribution of methane in the upper troposphere exhibits remarkable subseasonal variation in strong relation to the east-west oscillation of Asian Monsoon Anticyclone (AMA). Based on AMA mode composites, we confirm that the dynamic nature of the AMA, in terms of its subseasonal modes, modulates the horizonal distribution of methane as well as efficiency of vertical transport from the convective outflow upward to the upper
425 troposphere ~~structure of CH$_4$~~ over the monsoon region. In particular, the local coincidence of CH$_4$ emissions, strong convection and the location of the anticyclone around 80°E (WTP mode) favors the vertical transport of air from north India and Bangladesh to the upper troposphere, which contributes most significantly to the total CH$_4$ monsoon plume at the UT.~~AMA centering around 80°E (WTP mode) favors the vertical transport of air from north India and Bangladesh to the upper troposphere, which contributes most significantly to the total CH$_4$ monsoon plume at the UT~~. The methane source
430 from south China also contributes to the enhancement especially when AMA centering around 105°E (ETP mode). When the AMA center is located over the Iranian Plateau (around 60°E, IP mode), it is positioned far from the primary monsoon convective regions (e.g., the Indian subcontinent and the Bay of Bengal). In such a configuration, horizontal redistribution within the anticyclone becomes more dominant, rather than further vertical upwelling for these organized monsoon convective sources into the UTLS. ~~The vertical transport of methane is relatively weak with a horizonal redistribution at the~~
435 ~~UT when the AMA center moving around 60°E (IP mode).~~ Quantitively, the CH$_4$ anomaly in the UT under WTP mode is 50%-100% higher than that under the other modes, which show enhanced connection from key source region Himalayas-Gangetic Plain to the upper-level AMA.

Our study further reveals that methane enhancement at the upper troposphere over Asian summer monsoon region is a joint effect of monsoon transport system and annual emission peak at late August mainly from rice cultivation. The monsoon
440 dynamics consistently elevate upper tropospheric CH$_4$ 2%~10% throughout its whole course while emissions from rice cultivation notably contribute to the CH$_4$ peak commonly around late August. Our model sensitivity study reveals that, as to the monsoon seasonal and regional averaged methane amplitude in the UTLS region, the influence from conditions of AMA subseasonal oscillations is more remarkable than that from conditions of emissions.

Our findings underscore the importance of monsoon dynamics and its subseasonal variability in shaping the upper tropospheric methane 3-D distribution over the Asian monsoon region. Further research is encouraged to unravel the complexities of methane transport within the monsoon system, identify the primary source regions for methane emissions, and trace the trajectory of the monsoon methane plume after the monsoon's withdrawal.

## Data availability

All raw data can be provided by the corresponding authors upon request.

## Code availability

The GEOS-Chem model of atmospheric chemistry and transport model is maintained by Harvard University (http://geos-chem.seas.harvard.edu ). The ensemble Kalman filter code is publicly available at https://github.com/Rainbow1994/EnKF_CH4.git.

## Author contribution

MC designed the study; SZ performed the emission inversion, forward simulation and sensitivity tests; MC analyzed the data; MT and SZ wrote the manuscript draft; All the authors reviewed and edited the manuscript.

## Competing interests

The authors declare that they have no conflict of interest.

## Acknowledgments

We thank the GEOS-Chem community, in particular the Harvard University team which helps maintain the GEOS-Chem model, and the NASA Global Modelling and Assimilation Office (GMAO) for providing the MERRA2 data product.

## Financial support

This work was supported by the National Key R&D Program of China (no. 2022YFB3904802), by the National Natural Science Foundation of China (42105060), by the China Postdoctoral Science Foundation (E3442418), and by the Tibet Science and Technological Project (CGZH2023000385).

**References**

Alladi, H. K., Satheesh Chandran, P. R., and Ratnam, M. V.: Impact of ENSO on the UTLS chemical composition in the Asian Summer Monsoon Anticyclone, Atmos. Res., 309, 107551, https://doi.org/10.1016/j.atmosres.2024.107551, 2024.

Baker, A. K., Schuck, T. J., Brenninkmeijer, C. A. M., Rauthe-Schöch, A., Slemr, F., van Velthoven, P. F. J., and Lelieveld, J.: Estimating the contribution of monsoon-related biogenic production to methane emissions from South Asia using CARIBIC observations, Geophysical Research Letters, 39, https://doi.org/10.1029/2012GL051756, 2012.

Belikov, D. A., Saitoh, N., and Patra, P. K.: An Analysis of Interhemispheric Transport Pathways Based on Three-Dimensional Methane Data by GOSAT Observations and Model Simulations, JGR Atmospheres, 127, e2021JD035688, https://doi.org/10.1029/2021JD035688, 2022.

Bergman, J. W., Fierli, F., Jensen, E. J., Honomichl, S., and Pan, L. L.: Boundary layer sources for the Asian anticyclone: Regional contributions to a vertical conduit, JGR Atmospheres, 118, 2560–2575, https://doi.org/10.1002/jgrd.50142, 2013.

Bisht, J. S. H., Machida, T., Chandra, N., Tsuboi, K., Patra, P. K., Umezawa, T., Niwa, Y., Sawa, Y., Morimoto, S., Nakazawa, T., Saitoh, N., and Takigawa, M.: Seasonal Variations of SF6, CO2, CH4, and N2O in the UT/LS Region due to Emissions, Transport, and Chemistry, Journal of Geophysical Research: Atmospheres, 126, e2020JD033541, https://doi.org/10.1029/2020JD033541, 2021.

Bucci, S., Legras, B., Sellitto, P., D'Amato, F., Viciani, S., Montori, A., Chiarugi, A., Ravegnani, F., Ulanovsky, A., Cairo, F., and Stroh, F.: Deep-convective influence on the upper troposphere–lower stratosphere composition in the Asian monsoon anticyclone region: 2017 StratoClim campaign results, *Atmos. Chem. Phys.*, **20**, 12193–12210, https://doi.org/10.5194/acp-20-12193-2020, 2020.

Feng, L., Palmer, P., Boesch, H., and Dance, S.: Estimating surface CO2 fluxes from space-borne CO2 dry air mole fraction observations using an ensemble Kalman Filter, Atmospheric Chemistry and Physics, 9, 2619–2633, https://doi.org/10.5194/acp-9-2619-2009, 2009.

Feng, L., Palmer, P., Bosch, H., Parker, R., Webb, A., Correia, C., Deutscher, N., Domingues, L., Feist, D., Gatti, L., Gloor, M., Hase, F., Kivi, R., Liu, Y., Miller, J., Morino, I., Sussmann, R., Strong, K., Uchino, O., and Zahn, A.: Consistent regional fluxes of CH4 and CO2 inferred from GOSAT proxy XCH4 : XCO2 retrievals, 2010-2014, Atmospheric Chemistry and Physics, 17, 2017.

Garny, H. and Randel, W. J.: Dynamic variability of the Asian monsoon anticyclone observed in potential vorticity and correlations with tracer distributions, JGR Atmospheres, 118, https://doi.org/10.1002/2013JD020908, 2013.

Garny, H. and Randel, W. J.: Transport pathways from the Asian monsoon anticyclone to the stratosphere, Atmos. Chem. Phys., 16, 2703–2718, https://doi.org/10.5194/acp-16-2703-2016, 2016.

Gelaro, R., McCarty, W., Suárez, M. J., Todling, R., Molod, A., Takacs, L., Randles, C. A., Darmenov, A., Bosilovich, M. G., Reichle, R., Wargan, K., Coy, L., Cullather, R., Draper, C., Akella, S., Buchard, V., Conaty, A., Silva, A. M. da, Gu, W., Kim, G.-K., Koster, R., Lucchesi, R., Merkova, D., Nielsen, J. E., Partyka, G., Pawson, S., Putman, W., Rienecker, M., Schubert, S. D., Sienkiewicz, M., and Zhao, B.: The Modern-Era Retrospective Analysis for Research and Applications, Version 2 (MERRA-2), https://doi.org/10.1175/JCLI-D-16-0758.1, 2017.

von Hobe, M., Ploeger, F., Konopka, P., Kloss, C., Ulanowski, A., Yushkov, V., Ravegnani, F., Volk, C. M., Pan, L. L., Honomichl, S. B., Tilmes, S., Kinnison, D. E., Garcia, R. R., and Wright, J. S.: Upward transport into and within the Asian

monsoon anticyclone as inferred from StratoClim trace gas observations, Atmos. Chem. Phys., 21, 1267–1285, https://doi.org/10.5194/acp-21-1267-2021, 2021.

Krishnamurti, T. N. and Ardanuy, P.: The 10 to 20-day westward propagating mode and "Breaks in the Monsoons," Tellus A: Dynamic Meteorology and Oceanography, 32, 15, https://doi.org/10.3402/tellusa.v32i1.10476, 1980.

Krishnamurti, T. N. and Bhalme, H. N.: Oscillations of a Monsoon System. Part I. Observational Aspects, Journal of the Atmospheric Sciences, 33, 1937–1954, https://doi.org/10.1175/1520-0469(1976)033<1937:OOAMSP>2.0.CO;2, 1976.

Lau, W. K. M., Yuan, C., and Li, Z.: Origin, Maintenance and Variability of the Asian Tropopause Aerosol Layer (ATAL): The Roles of Monsoon Dynamics, Sci Rep, 8, 3960, https://doi.org/10.1038/s41598-018-22267-z, 2018.

Legras, B. and Bucci, S.: Confinement of air in the Asian monsoon anticyclone and pathways of convective air to the stratosphere during the summer season, Atmos. Chem. Phys., 20, 11045–11064, https://doi.org/10.5194/acp-20-11045-2020, 2020.

Luo, J., Pan, L. L., Honomichl, S. B., Bergman, J. W., Randel, W. J., Francis, G., Clerbaux, C., George, M., Liu, X., and Tian, W.: Space–time variability in UTLS chemical distribution in the Asian summer monsoon viewed by limb and nadir satellite sensors, Atmos. Chem. Phys., 18, 12511–12530, https://doi.org/10.5194/acp-18-12511-2018, 2018.

Machida, T., Matsueda, H., Sawa, Y., Niwa, Y., Tsuboi, K., Ishijima, K., Katsumata, K., Murayama, S., Morimoto, S., Goto, D., Aoki, S., and Sasakawa, M.: Atmospheric trace gas data from the CONTRAIL flask air sampling, ver.2023.1.0 (ver.2023.1.0), https://doi.org/10.17595/20230725.001, 2023.

Manney, G. L., Santee, M. L., Lawrence, Z. D., Wargan, K., and Schwartz, M. J.: A Moments View of Climatology and Variability of the Asian Summer Monsoon Anticyclone, Journal of Climate, 34, 7821–7841, https://doi.org/10.1175/JCLI-D-20-0729.1, 2021.

Murray, L., Fiore, A., Shindell, D., Naik, V., and Horowitz, L.: Large uncertainties in global hydroxyl projections tied to fate of reactive nitrogen and carbon, Proceedings of the National Academy of Sciences of the United States of America, 118, https://doi.org/10.1073/pnas.2115204118, 2021.

Nützel, M., Dameris, M., and Garny, H.: Movement, drivers and bimodality of the South Asian High, Atmospheric Chemistry and Physics, 16, 14755–14774, https://doi.org/10.5194/acp-16-14755-2016, 2016.

Pan, L. L., Honomichl, S. B., Kinnison, D. E., Abalos, M., Randel, W. J., Bergman, J. W., and Bian, J.: Transport of chemical tracers from the boundary layer to stratosphere associated with the dynamics of the Asian summer monsoon, JGR Atmospheres, 121, https://doi.org/10.1002/2016JD025616, 2016.

Pan, L. L., Kinnison, D., Liang, Q., Chin, M., Santee, M. L., Flemming, J., Smith, W. P., Honomichl, S. B., Bresch, J. F., Lait, L. R., Zhu, Y., Tilmes, S., Colarco, P. R., Warner, J., Vuvan, A., Clerbaux, C., Atlas, E. L., Newman, P. A., Thornberry, T., Randel, W. J., and Toon, O. B.: A Multimodel Investigation of Asian Summer Monsoon UTLS Transport Over the Western Pacific, JGR Atmospheres, 127, e2022JD037511, https://doi.org/10.1029/2022JD037511, 2022.

Pan, L. L., Atlas, E. L., Honomichl, S. B., Smith, W. P., Kinnison, D. E., Solomon, S., Santee, M. L., Saiz-Lopez, A., Laube, J. C., Wang, B., Ueyama, R., Bresch, J. F., Hornbrook, R. S., Apel, E. C., Hills, A. J., Treadaway, V., Smith, K., Schauffler, S., Donnelly, S., … Newman, P. A.: East Asian summer monsoon delivers large abundances of very short-lived organic chlorine substances to the lower stratosphere, *Proc. Natl. Acad. Sci. USA*, **121**, e2318716121, https://doi.org/10.1073/pnas.2318716121, 2024.

Park, M., Randel, W. J., Kinnison, D. E., Garcia, R. R., and Choi, W.: Seasonal variation of methane, water vapor, and nitrogen oxides near the tropopause: Satellite observations and model simulations, J. Geophys. Res., 109, 2003JD003706, https://doi.org/10.1029/2003JD003706, 2004.

545 Park, M., Randel, W. J., Emmons, L. K., and Livesey, N. J.: Transport pathways of carbon monoxide in the Asian summer monsoon diagnosed from Model of Ozone and Related Tracers (MOZART), J. Geophys. Res., 114, 2008JD010621, https://doi.org/10.1029/2008JD010621, 2009.

Parker, R., Webb, A., Boesch, H., Kalaitzi, N., Bergamaschi, P., Chevallier, F., Palmer, P., Feng, L., Griffith, D., Hase, F., Kivi, R., Oh, Y.-S., Ohyama, H., Pollard, D., Roehl, C., Sha, M., Shiomi, K., Strong, K., Té, Y., and Barrio Guilló, R.: A 550 Decade of GOSAT Proxy Satellite CH4 Observations, https://doi.org/10.5194/essd-2020-114, 2020.

Ploeger, F., Gottschling, C., Griessbach, S., Grooß, J.-U., Guenther, G., Konopka, P., Müller, R., Riese, M., Stroh, F., Tao, M., Ungermann, J., Vogel, B., and von Hobe, M.: A potential vorticity-based determination of the transport barrier in the Asian summer monsoon anticyclone, Atmos. Chem. Phys., 15, 13145–13159, https://doi.org/10.5194/acp-15-13145-2015, 2015

555 Ploeger, F., Konopka, P., Walker, K., and Riese, M.: Quantifying pollution transport from the Asian monsoon anticyclone into the lower stratosphere, Atmospheric Chemistry and Physics, 17, 7055–7066, https://doi.org/10.5194/acp-17-7055-2017, 2017.

Randel, W. J., Park, M., Emmons, L., Kinnison, D., Bernath, P., Walker, K. A., Boone, C., and Pumphrey, H.: Asian Monsoon Transport of Pollution to the Stratosphere, Science, 328, 611–613, https://doi.org/10.1126/science.1182274, 2010.

560 Riese, M., Ploeger, F., Rap, A., Vogel, B., Konopka, P., Dameris, M., and Forster, P.: Impact of uncertainties in atmospheric mixing on simulated UTLS composition and related radiative effects, J. Geophys. Res., 117, 2012JD017751, https://doi.org/10.1029/2012JD017751, 2012.

Rohs, S., Schiller, C., Riese, M., Engel, A., Schmidt, U., Wetter, T., Levin, I., Nakazawa, T., and Aoki, S.: Long-term changes of methane and hydrogen in the stratosphere in the period 1978–2003 and their impact on the abundance of 565 stratospheric water vapor, J. Geophys. Res., 111, 2005JD006877, https://doi.org/10.1029/2005JD006877, 2006.

Rosenlof, K. H., Tuck, A. F., Kelly, K. K., Russell, J. M., and McCormick, M. P.: Hemispheric asymmetries in water vapor and inferences about transport in the lower stratosphere, J. Geophys. Res., 102, 13213–13234, https://doi.org/10.1029/97JD00873, 1997.

Saito, R., Patra, P. K., Sweeney, C., Machida, T., Krol, M., Houweling, S., Bousquet, P., Agusti-Panareda, A., Belikov, D., 570 Bergmann, D., Bian, H., Cameron-Smith, P., Chipperfield, M. P., Fortems-Cheiney, A., Fraser, A., Gatti, L. V., Gloor, E., Hess, P., Kawa, S. R., Law, R. M., Locatelli, R., Loh, Z., Maksyutov, S., Meng, L., Miller, J. B., Palmer, P. I., Prinn, R. G., Rigby, M., and Wilson, C.: TransCom model simulations of methane: Comparison of vertical profiles with aircraft measurements, Journal of Geophysical Research: Atmospheres, 118, 3891–3904, https://doi.org/10.1002/jgrd.50380, 2013.

Schuck, T. J., Brenninkmeijer, C. A. M., Baker, A. K., Slemr, F., Von Velthoven, P. F. J., and Zahn, A.: Greenhouse gas 575 relationships in the Indian summer monsoon plume measured by the CARIBIC passenger aircraft, Atmos. Chem. Phys., 10, 3965–3984, https://doi.org/10.5194/acp-10-3965-2010, 2010.

Schuldt, K. N., Aalto, T., Andrews, A., Aoki, S., Apadula, F., Arduini, J., Arlyn Andrews, Baier, B., Bartyzel, J., Bergamaschi, P., Biermann, T., Biraud, S. C., Boenisch, H., Brailsford, G., Brand, W. A., Van Der Veen, C., Chen, H., Myhre, C. L., Couret, C., Miller, C. E., Choong-Hoon Lee, Lunder, C. R., Plass-Duelmer, C., Plass-Duelmer, C., Gerbig, C., 580 Sloop, C. D., Sweeney, C., Kubistin, D., Goto, D., Jaffe, D., Heltai, D., Lowry, D., Munro, D., Worthy, D., Dlugokencky, E.,

Kozlova, E., Gloor, E., Cuevas, E., Hintsa, E., Kort, E., Morgan, E., Nisbet, E., Obersteiner, F., Apadula, F., Meinhardt, F., Moore, F., Vitkova, G., Giordane A. Martins, Manca, G., Zazzeri, G., Brailsford, G., Forster, G., Santoni, G., Haeyoung Lee, Boenisch, H., Moossen, H., Timas, H., Matsueda, H., Kang, H.-Y., Huilin Chen, Lehner, I., Mammarella, I., Bartyzel, J., Elkins, J. W., Jaroslaw Necki, Pittman, J., Pichon, J. M., Müller-Williams, J., Jgor Arduini, Turnbull, J., Miller, J. B., Lee, J., Jooil Kim, Pitt, J., DiGangi, J. P., Lavric, J., Hatakka, J., Worsey, J., Holst, J., Lehtinen, K., Kominkova, K., McKain, K., Saito, K., Davis, K., Thoning, K., Tørseth, K., Haszpra, L., Sørensen, L. L., Gatti, L. V., Emmenegger, L., Sha, M. K., Menoud, M., Delmotte, M., Fischer, M. L., De Vries, M., Schumacher, M., Torn, M., Popa, M. E., Leuenberger, M., et al.: Multi-laboratory compilation of atmospheric methane data for the period 1983-2021; obspack_ch4_1_GLOBALVIEWplus_v5.0_2022-10-17, https://doi.org/10.25925/20221001, 2022.

Siu, L. W. and Bowman, K. P.: Unsteady Vortex Behavior in the Asian Monsoon Anticyclone, Journal of the Atmospheric Sciences, 77, 4067–4088, https://doi.org/10.1175/JAS-D-19-0349.1, 2020.

Stanevich, I., Jones, D. B. A., Strong, K., Parker, R. J., Boesch, H., Wunch, D., Notholt, J., Petri, C., Warneke, T., Sussmann, R., Schneider, M., Hase, F., Kivi, R., Deutscher, N. M., Velazco, V. A., Walker, K. A., and Deng, F.: Characterizing model errors in chemical transport modeling of methane: impact of model resolution in versions v9-02 of GEOS-Chem and v35j of its adjoint model, Geoscientific Model Development, 13, 3839–3862, https://doi.org/10.5194/gmd-13-3839-2020, 2020.

Stanevich, I., Jones, D. B. A., Strong, K., Keller, M., Henze, D. K., Parker, R. J., Boesch, H., Wunch, D., Notholt, J., Petri, C., Warneke, T., Sussmann, R., Schneider, M., Hase, F., Kivi, R., Deutscher, N. M., Velazco, V. A., Walker, K. A., and Deng, F.: Characterizing model errors in chemical transport modeling of methane: using GOSAT XCH$_4$ data with weak-constraint four-dimensional variational data assimilation, Atmospheric Chemistry and Physics, 21, 9545–9572, https://doi.org/10.5194/acp-21-9545-2021, 2021.

Stavert, A. R., Saunois, M., Canadell, J. G., Poulter, B., Jackson, R. B., Regnier, P., Lauerwald, R., Raymond, P. A., Allen, G. H., Patra, P. K., Bergamaschi, P., Bousquet, P., Chandra, N., Ciais, P., Gustafson, A., Ishizawa, M., Ito, A., Kleinen, T., Maksyutov, S., McNorton, J., Melton, J. R., Müller, J., Niwa, Y., Peng, S., Riley, W. J., Segers, A., Tian, H., Tsuruta, A., Yin, Y., Zhang, Z., Zheng, B., and Zhuang, Q.: Regional trends and drivers of the global methane budget, Global Change Biology, 28, 182–200, https://doi.org/10.1111/gcb.15901, 2022.

Tao, M., Cai, Z., Zhu, S., Liu, Y., Feng, L., Fang, S., Yi, Y., and Bian, J.: New evidence for CH 4 enhancement at upper troposphere associated with Asian summer monsoon, Environmental Research Letters, 19, https://doi.org/10.1088/1748-9326/ad2738, 2024.

The International GEOS-Chem User Community: Geoschem/geos-chem: GEOS-Chem 12.5.0, 2019.

Tomsche, L., Pozzer, A., Ojha, N., Parchatka, U., Lelieveld, J., and Fischer, H.: Upper tropospheric CH<sub>4</sub> and CO affected by the South Asian summer monsoon during the Oxidation Mechanism Observations mission, Atmos. Chem. Phys., 19, 1915–1939, https://doi.org/10.5194/acp-19-1915-2019, 2019.

Total Carbon Column Observing Network (TCCON) Team: 2020 TCCON Data Release, https://doi.org/10.14291/TCCON.GGG2020, 2022.

Vogel, B., Müller, R., Günther, G., Spang, R., Hanumanthu, S., Li, D., Riese, M., and Stiller, G. P.: Lagrangian simulations of the transport of young air masses to the top of the Asian monsoon anticyclone and into the tropical pipe, Atmos. Chem. Phys., 19, 6007–6034, https://doi.org/10.5194/acp-19-6007-2019, 2019.

Vogel, B., Volk, C. M., Wintel, J., Lauther, V., Clemens, J., Grooß, J.-U., Günther, G., Hoffmann, L., Laube, J. C., Müller, R., Ploeger, F., and Stroh, F.: Evaluation of vertical transport in ERA5 and ERA-Interim reanalysis using high-altitude

620 aircraft measurements in the Asian summer monsoon 2017, Atmos. Chem. Phys., 24, 317–343, https://doi.org/10.5194/acp-24-317-2024, 2024.

Xiong, X., Houweling, S., Wei, J., Maddy, E., Sun, F., and Barnet, C.: Methane plume over south Asia during the monsoon season: satellite observation and model simulation, Atmos. Chem. Phys., 9, 783–794, https://doi.org/10.5194/acp-9-783-2009, 2009.

625 Yan, X., Konopka, P., Ploeger, F., Podglajen, A., Wright, J. S., Müller, R., and Riese, M.: The efficiency of transport into the stratosphere via the Asian and North American summer monsoon circulations, Atmos. Chem. Phys., 19, 15629–15649, https://doi.org/10.5194/acp-19-15629-2019, 2019.

Yu, P., Rosenlof, K. H., Liu, S., Telg, H., Thornberry, T. D., Rollins, A. W., Portmann, R. W., Bai, Z., Ray, E. A., Duan, Y., Pan, L. L., Toon, O. B., Bian, J., and Gao, R.-S.: Efficient transport of tropospheric aerosol into the stratosphere via the 630 Asian summer monsoon anticyclone, Proc. Natl. Acad. Sci. U.S.A., 114, 6972–6977, https://doi.org/10.1073/pnas.1701170114, 2017.

Zeng, Z.-C., Byrne, B., Gong, F.-Y., He, Z., and Lei, L.: Correlation between paddy rice growth and satellite-observed methane column abundance does not imply causation, Nat Commun, 12, 1163, https://doi.org/10.1038/s41467-021-21434-7, 2021.

635 Zhang, G., Xiao, X., Dong, J., Xin, F., Zhang, Y., Qin, Y., Doughty, R. B., and Moore, B.: Fingerprint of rice paddies in spatial–temporal dynamics of atmospheric methane concentration in monsoon Asia, Nat Commun, 11, 554, https://doi.org/10.1038/s41467-019-14155-5, 2020.

Zhang, Q., Wu, G., and Qian, Y.: The Bimodality of the 100 hPa South Asia High and its Relationship to the Climate Anomaly over East Asia in Summer., Journal of the Meteorological Society of Japan, 80, 733–744, 640 https://doi.org/10.2151/jmsj.80.733, 2002.

Zhao, Y., Saunois, M., Bousquet, P., Lin, X., Berchet, A., Hegglin, M. I., Canadell, J. G., Jackson, R. B., Hauglustaine, D. A., Szopa, S., Stavert, A. R., Abraham, N. L., Archibald, A. T., Bekki, S., Deushi, M., Jöckel, P., Josse, B., Kinnison, D., Kirner, O., Marécal, V., O'Connor, F. M., Plummer, D. A., Revell, L. E., Rozanov, E., Stenke, A., Strode, S., Tilmes, S., Dlugokencky, E. J., and Zheng, B.: Inter-model comparison of global hydroxyl radical (OH) distributions and their impact 645 on atmospheric methane over the 2000–2016 period, Atmospheric Chemistry and Physics, 19, 13701–13723, https://doi.org/10.5194/acp-19-13701-2019, 2019.

Zhu, S., Feng, L., Liu, Y., Wang, J., and Yang, D.: Decadal Methane Emission Trend Inferred from Proxy GOSAT XCH4 Retrievals: Impacts of Transport Model Spatial Resolution, Advances in Atmospheric Sciences, 39, https://doi.org/10.1007/s00376-022-1434-6, 2022.

650